Published in final edited form as:
Magn Reson Med. 2013 November ; 70(5): 1241–1250. doi:10.1002/mrm.24570.

Optimized 3D Ultrashort Echo Time Pulmonary MRI

Kevin M. Johnson[1,*], **Sean B. Fain**[1,2,3], **Mark L. Schiebler**[1], and **Scott Nagle**[1,2]

[1]Department of Medical Physics, University of Wisconsin, Madison, Wisconsin, USA.

[2]Department of Radiology, University of Wisconsin, Madison, Wisconsin, USA.

[3]Department of Biomedical Engineering, University of Wisconsin, Madison, Wisconsin, USA.

Abstract

Purpose—To optimize 3D radial ultrashort echo time MRI for high resolution whole-lung imaging.

Methods—3D radial ultrashort echo time was implemented on a 3T scanner to investigate the effects of: (1) limited field-of-view excitation, (2) variable density readouts, and (3) radial oversampling. Improvements in noise performance and spatial resolution were assessed through simulation and phantom studies. Their effects on lung and airway visualization in five healthy male human subjects (mean age 32 years) were compared qualitatively through blinded ordinal scoring by two cardiothoracic radiologists using a nonparametric Friedman test ($P < 0.05$). Relative signal difference between endobronchial air and adjacent lung tissue, normalized to nearby vessel, was used as a surrogate for lung tissue signal. Quantitative measures were compared using the paired Student's *t*-test ($P < 0.05$). Finally, clinical feasibility was investigated in a patient with interstitial fibrosis.

Results—Simulation and phantom studies showed up to 67% improvement in SNR and reduced blurring for short T2* species using all three optimizations. In vivo images showed decreased artifacts and improved lung tissue and airway visualization both qualitatively and quantitatively.

Conclusion—The use of limited field-of-view excitation, variable readout gradients, and radial oversampling significantly improve the technical quality of 3D radial ultrashort echo time lung images.

Keywords

MRI; lung; ultrashort echo time; radial imaging

Magnetic resonance imaging (MRI) holds potential to provide safe and comprehensive assessment of lung disease. MRI techniques now exist to measure ventilation and parenchyma microstructure with hyperpolarized He^3 (1,2) and Xe^{129} gas (3,4), gadolinium contrast enhanced (5) and noncontrast(6) perfusion, pulmonary angiography, and pulmonary flow (7). Additionally, emerging techniques hold promise for the assessment of pulmonary

[*]Correspondence to: Kevin M. Johnson, Ph.D., Department of MR/CT Research, University of Wisconsin-Madison, 1122l Wisconsin Institutes Medical Research, 1111 Highland Ave., Madison, WI 53705-2275. kmjohnson3@wisc.edu.

cellular metabolism with hyperpolarized C^{13}-labeled tracers (8) and inflammation with F^{19} (9) or super paramagnetic iron oxide particles (SPIOs) (10). Despite this array of promising techniques for assessing lung function, structural lung imaging with MRI has proven to be challenging. Traditional MR techniques for anatomical assessment are largely hindered by short transverse relaxation times [$T2$ ~ 80 ms, $T2^*$ ~ 0.5–3 ms (11–15)], low proton density, and the presence of respiratory and cardiac motion. Subsequently, structural proton-based lung MRI has seen limited success.

Short echo time (TE) has been shown to be crucial to maintaining image quality in the lungs (16,17). With short echo times, fast spin echo sequences show clinical utility for the assessment of nonsmall cell lung cancer (18), diffuse lung disease (19), and pulmonary edema (20). However, due to $T2$ blurring and low acquisition efficiency, fine-scale structures of the lung are not generally well-visualized. This has sparked substantial interest in sequences that provide near zero echo times, such as ultrashort TE (UTE), swept Fourier (SWIFT) (21) imaging, zero TE techniques [e.g. ZTE (22) and WASPI (23)], single point imaging techniques [e.g. SPRITE (24)), and hybrid techniques (e.g. PETRA (25) and AWSOS (26)]. However, despite attempts dating back to the early 90's (17), lung imaging with these techniques has only recently seen significant progress. In small animal studies, UTE sequences have now demonstrated high resolution morphologic lung imaging (27–29), inflammation (10), oxygen-enhanced ventilation, contrast-enhanced perfusion (30), and $T2^*$ mapping (31).

Clinical translation of UTE and other short $T2^*$ imaging techniques to humans remains highly challenging. Conventionally, these sequences utilize short repetition time (TR) free induction decay sampling that limits signal recovery for species with long longitudinal relaxation times ($T1$), such as the lung parenchyma [$T1$ ~ 1200 ms (32)]. Furthermore, low proton density and limited breath-hold times further reduce signal levels for parenchymal and airway structures. Thus, previous human studies have used relatively thick slice 2D breath-hold UTE sequences (12,17,33) that provide limited spatial coverage and are highly susceptible to inflow related artifacts (33). 3D UTE has several potential advantages over 2D UTE approaches and has seen substantial success in animal models (10,27–31). These include a more efficient radiofrequency (RF) excitation, isotropic spatial resolution with full chest coverage similar to computed tomography (CT), and reduced sensitivity to structured motion artifacts (34). Unfortunately, 3D radial UTE is impractical to perform in a single breath-hold and provides lower SNR efficiency than 2D radial sampling (35). Free breathing motion compensation methods are not easily adapted to 3D lung imaging and respiratory gating or triggering is necessary, typically either with an external respiratory bellows (36,37) or using a navigator pulse (38).

3D imaging of short $T2$ is further limited by challenges with short $T2$ excitation. Excitation schemes for short $T2$, 3D imaging must provide high bandwidth excitation and minimize $T2$ decay between excitation and acquisition. Suitable schemes include hard RF pulses, frequency swept RF pulses (21), and half pulses (39). Of these techniques, only half pulses provide spatial selectivity but at the cost of (1) increased susceptibility to eddy currents and $T2$ decay and (2) increased scan time due to the necessity of two excitations per k-space trajectory (40). As an alternative, quadratic phase outer volume suppression can be

performed before excitation (41); however, this substantially increases RF power requirements and specific absorption rate (SAR). Subsequently, 3D short *T*2 imaging is most often performed with hard RF excitation. This forces the imaging FOV to be much larger than the area of interest and/or excites spins well outside the FOV where the gradient non-linearity and B_0 inhomogeneity cause artifacts.

The purpose of this study was to optimize the 3D radial UTE technique for lung imaging to improve the SNR and image quality. This will allow future translational studies exploring the utility of combined structural and functional MRI in specific patient populations, potentially avoiding the need for CT and its associated radiation burden. Specifically, we hypothesized that the following techniques would improve the SNR and image quality of 3D radial UTE MRI of the lungs: (1) limited field-of-view (FOV) excitation, (2) variable readout gradients with eddy-current corrections, and (3) radial over-sampling. These techniques were first evaluated through simulation and phantom studies. A small pilot study in five healthy human subjects was also performed to illustrate the technical feasibility of using these methods along with a novel adaptive respiratory respiratory gating method in vivo to perform high-resolution anatomical imaging of human lungs.

METHODS

Pulse Sequence

Figure 1 shows an overview of the 3D radial UTE pulse sequence with an oversampled, variable density readout.

Readout Trajectory and Corrections—Traditionally, center-out radial sampling with trapezoidal gradients has been utilized for UTE acquisitions. This trajectory collects a half line in k-space in a time-efficient fashion, but can be sensitive to gradient errors and provides low signal-to-noise (SNR) efficiency. SNR inefficiency arises from non-uniform sampling density (35). The efficiency relative to uniform sampling, η, can be computed:

$$\eta = \frac{\sum d_i}{\sqrt{N \sum d_i^2}}, \quad [1]$$

where d_i is density compensation function for each *k*-space sample and *N* is the number of samples. This is minimized when d_i is uniform. For a 3D radial trajectory with k^2 sampling density compensation, this inefficiency results in a 25.5% reduction in SNR (42). This loss can be compensated through the use of variable density gradients (43,44). In the context of ^{23}Na imaging, these techniques have been shown to provide images with higher SNR and reduced blurring (42,45,46) compared to standard ramp sampled trapezoid gradients. However, these techniques have not been applied to proton MRI techniques.

To facilitate improved design of SNR-optimized gradients in a flexible framework, we design gradients with a discrete arc length formulation (47). This modified algorithm allows (1) incorporation of arbitrary density compensation functions and sampling patterns, (2) automatically chooses optimal parameters for a given readout length, and (3) provides more optimal waveforms in slew limited cases. In this formulation, trajectories are first

parameterized from k-space into arc length, *s*. Subsequently the optimal trajectory is determined based upon a position-dependent slew limitation (47) and variable density gradient strength limitations:

$$g(s) < min\left(\left|\frac{A}{COV(s,I)}\right|, G_{max}\right), \quad [2]$$

where *g* is the gradient strength, *s* is the position along the arc, *A* is an arbitrary scaling factor, COV is the covariance, $G_{\max}$ is the maximum gradient strength, and *I* is the final image. For gridding reconstructions, COV(*s*,*I*) is equivalent to the sampling density correction utilized during reconstruction and is equal to s^2 in the case of center-out radial imaging with analytical sampling density compensation:

$$g(s) < min\left(\left|\frac{A}{s^2}\right|, G_{max}\right). \quad [3]$$

A scales the noise covariance to a desired gradient strength and subsequently controls the total duration of the readout. *A* is initially set to $G_{\max} \cdot \max(\mathrm{COV}(s,I))$. In this case, the desired gradient is always greater than $G_{\max}$ and the algorithm will produce the time-optimal gradient (i.e. a trapezoid). Subsequent iterations reduce A until the readout time is greater than or equal to the desired time. To allow rapid computation, this is performed with a simple multi-resolution search. For realistic readout lengths, this operation takes less than a second to obtain 4 μs accuracy using a desktop computer (Intel i7 860). Figure 1 shows an example with out-and-back sampling to collect ultrashort (0.08 ms) and conventional (2.1 ms) echo time images.

The increased slewing of variable density readouts has the potential to increase eddy currents and sensitivity to timing errors. Similar errors are also seen with trapezoid gradients and can dramatically lower the spatial resolution and SNR for short *T*2 or *T*2* structures in the lung (48). To compensate for these eddy currents and timing errors, we utilize per-subject thin slice calibrations (49,50) to estimate gradient and B_0 eddy current terms. This calibration is performed immediately following the acquisition and used to retrospectively correct k-space positions and to perform global B_0 demodulation.

Limiting the Field of View—The effective flip angle experienced by a short *T*2 species can be derived from Bloch equations and is well developed for constant amplitude RF pulses (51–54). The excitation performance of selective excitations can be derived utilizing a similar framework. For species with long *T*1, assuming full recovery, the flip angle is approximately equal to the frequency domain overlap of the Lorentzian distribution and that of the Fourier transform of the RF pulse:

$$M_z(T2) \approx M_0 \int_{-\infty}^{\infty} cos(\alpha(s))\,\Omega(f)\,df. \quad [4]$$

where α is the flip angle as a function of frequency is derived from Bloch simulations, M_0 is the initial magnetization, γ is the gyromagnetic ratio, Ψ is the normalized spin distribution function (Lorentzian), and *f* is the frequency. From this, it is immediately recognized that the RF pulse bandwidth must be greater than the line width of the species of interest in order to

provide efficient excitation. This describes the effect on longitudinal magnetization, which is independent of phase imparted to spins with different off resonant frequencies. The detectable signal, *S* at the end of the RF pulse is approximately:

$$S \approx M_0 \int_{-\infty}^{\infty} sin\left(\alpha\left(s\right)\right) e^{i\varphi(s)} \Omega\left(f\right) df. \quad [5]$$

where φ is the imparted phase of the RF pulse as a function of frequency. Thus, RF pulses must impart minimal phase within the pass band to allow signal detection. For large excitation slabs, both high bandwidth and minimum imparted phase can be achieved with short, minimum-phase Shinnar-LeRoux (SLR) RF-pulses.

Minimum phase RF pulses were compared to hard and windowed Sinc excitations in Bloch simulations. Minimum phase RF pulses were designed for a 300 μs excitation, nominal bandwidth of 30 kHz, and 4% ripple in stop and pass bands. A symmetric, Hann windowed sinc was subsequently designed to achieve identical peak B1 and pulse width. Bloch simulations were performed for a 6° nominal flip angle to compare the excitation and signal efficiency with pulse width ranging from 10 μs to 5 ms. Simulations assumed no *T*1 decay and a *T*2 of 0.5 ms, a conservative estimate of *T*2* in the lungs. For sinc and SLR pulse, slice profiles were computed for a 28 cm selective excitation and measurements of fractional transition width were made.

Even with slab selection, spins may still be excited outside the FOV (e.g. patient arms, excitation side lobes). Since each radial readout is low pass filtered to the prescribed FOV, signal from these spins will lead to artifacts similar to computed tomography (CT) truncation artifacts. To prevent these artifacts, the readout sampling rate was doubled to effectively double the imaging FOV. This comes at the expense of increased data storage requirements, but since all data are used for reconstruction, there is no noise penalty.

Respiratory Gating—For 3D UTE, the long scan time makes it impractical to use breath-hold acquisitions. Therefore, an adaptive respiratory gating method using a respiratory bellows signal was used (Fig. 2). This method has been shown to be robust to respiratory drift and irregular breathing patterns in the setting of renal angiography (36,37). Every TR, the bellows signal is analyzed to continuously adapt the gating based on the last 10 s of data. This is achieved by sorting the bellows signal in a histogram and setting an acceptance window. In this work, we utilize a simple 50% threshold to accept end expiratory data and reject inspiratory data. If the bellows position is beyond the threshold, data is not stored and the same *k*-space trajectory is repeated until the bellows position is below the threshold. To mitigate the possibility of structured artifacts from cardiac and residual respiratory motion, we acquire projections with psuedo-random view ordering determined by a 2D bit-reverse algorithm.

Simulations and Phantoms

All experiments assumed the performance or utilized a clinical 3T scanner (MR750, GE Healthcare, Waukesha, WI, Max slew = 200 T/m/s, Max gradient = 50 mT/m). Digital phantom simulations were first performed to evaluate the effect of variable density gradients with respect to *T*2* blurring and SNR performance. Images were simulated using the

analytical *k*-space values for a cylinder with 12 mm diameter. Both variable density and conventional trapezoid gradients were designed with a 1 ms readout and 0.7 mm isotropic resolution images. For variable density gradient design the max gradient strength (G_{max}) was set to 18.4 mT/m corresponding to a required sampling rate of ±125 Hz for a 32 cm FOV. For trapezoid gradients, the 1 ms duration required a gradient strength of 9.7 mT/m, approximately 7.5μs/sample, with an 88 μs ramp time. Simulated $R2^*$ values ranged from 0 to 10,000 s^{-1} ($T2^*$ = 0.1 to ∞ ms). From these images, the spatial resolution was estimated from the edge width that was evaluated between the 25% and 75% maximum values. SNR was evaluated from 100 realizations with independent, complex, zero-mean Gaussian noise added to the *k*-space data with a standard deviation equal to 1% of the maximum value in *k*-space.

Phantoms were created consisting of 5 mL glass vials filled with varying concentrations of gadopentetate dime-glumine (Magnevist, Bayer, Wayne, NJ) : 250, 166, 100, 55, and 12 mM. The nominal dimensions of these vials were 12.7 mm (O.D) × 11.3 mm (I.D) × 40 mm (length). Vials were placed in a water bath of deionized water and ten consecutive images were acquired with variable density and trapezoid gradients identical to those utilized for digital simulations. Relevant scan parameters included: 0.7 mm isotropic resolution, $TE_1/TE_2/TR$ = 0.080/2.1/4.2 ms, RF spoiling, flip angle = 5° , scan-time = 2:46 min, eight-channel head coil (HD Brain, GE Healthcare, Waukesha, WI) and 39,816 radial projections. Immediately following acquisition, thin slice gradient calibrations were performed for both trapezoid and variable density gradients requiring 10 s of additional time. Images were reconstructed at 0.17 mm isotropic resolution with an optimized gridding routine and analytical density compensation (55) . $T2^*$ maps were estimated utilizing a two-point complex least squares fitting of the short and long echo time images. Subsequently, regions of interest (ROI) were drawn in the short and long echo time maps from a slice at the midpoint of the vial. SNR was estimated from the standard deviation from 10 repeated scans using an ROI placed in the vial and normalized to the SNR in the long $T2^*$ phantom (~11.6 ms) acquired with variable density sampling. To assess spatial resolution, the edge width was measured using 25% and 75% maximum thresholds for each vial as was the case for the digital simulations.

Human Comparison Study

Using a HIPAA-compliant, IRB-approved protocol, five subjects were recruited and scanned on a 3T clinical scanner (GE MR750, GE Healthcare, Waukesha, WI) without hardware modification. Subjects were recruited from an healthy subject database and had no known disease at time of recruitment. Informed written consent was obtained from all subjects. Three acquisitions were performed on each subject: (1) 40μs non-selective hard RF pulse, no radial oversampling, and ramp-sampled trapezoid readouts, (2) axially-selective RF pulse, radial oversampling, and ramp-sampled trapezoid readouts, and (3) axially-selective RF pulse, radial oversampling, and variable density readouts. For all acquisitions, a 1 ms readout duration was utilized. This readout duration is slightly greater than the expect $T2^*$ of lung tissue at 3T. Some blurring of fine lung structures is subsequently expected; however, SNR will be improved in larger structures. For variable density gradient design the max gradient strength (G_{max}) was set to 18.4 mT/m corresponding to a required sampling

rate of ±125 Hz for a 32 cm FOV. For trapezoid gradients, the 1 ms duration required a gradient strength of 9.7 mT/m, ~7.5μs/sample, with an 88 μs ramp time. All images were collected with adaptive respiratory gating using a 50% acceptance window. Other relevant parameters included: 1.25 mm isotropic resolution, 32 × 32 × 32 cm^3 FOV, $TE_1/TE_2/TR$ = 0.080/2.1/4.1 ms, flip angle = 6°, twenty channel phased array coil (Torso Array, Neocoil, Pewuakee, WI, USA), nominal scan time = 9:18 min. No intravenous contrast was administered. Images were reconstructed at 0.83 mm iso-tropic resolution using iterative non-Cartesian SENSE (56) with coil sensitivities estimated from the central over-sampled center of *k*-space for the first echo (57).

Image Analysis

Regions of interest (ROI) were manually drawn in the right main bronchus and nearby lung tissue and large vessels for each dataset. Subsequently, the difference between air and lung tissue signal normalized to vessel signal was used as a normalized contrast ratio, C_R, and was calculated:

$$C_R = \frac{Lung - Airway}{Vessel}. \quad [6]$$

Additionally, the same ROI's were utilized to estimate the “apparent signal to noise” ratio:

$$S_R = \sqrt{\frac{2}{\pi}} \frac{Lung}{Airway}. \quad [7]$$

Due to the nonuniform noise distribution and undersampling, this is a mixed metric of both stochastic noise and image artifacts. A paired Student's t-test was used to assess differences between the three acquisitions for both C_R and S_R. For qualitative evaluations, axial and coronal reformatted volumes of the first echo were presented in a randomized order and evaluated using consensus methodology by two cardiothoracic radiologists. The Likert scale used for grading these images is shown in Table 1. Individual scores were assigned for artifacts from blurring, cardiac motion, streaks and noise, and image quality of lung tissue and airways. Large (segmental and larger) and small (subsegmental and smaller) airways received separate scores. Readers were blinded to the acquisition type. Statistical differences in image quality between the three acquisitions were assessed for each patient with a nonparametric Friedman test. Statistical significance was set at the $P < 0.05$ level for all comparisons.

Feasibility in Interstitial Fibrosis

To provide initial clinical feasibility, a single, 74-year-old, female subject with a history of mixed connective tissue disease undergoing a clinical cardiac MRI was recruited for imaging using a HIPAA-compliant, IRB-approved protocol. Due to scan time and setup limitations, 3D UTE images were only collected using selective excitation, radial oversampling, and variable density readouts, a shorter 5:30 scan time with a higher degree of radial undersampling, and an eight channel phased array coil (HD Cardiac, GE Healthcare, Waukesha, WI, USA). All other parameters, including scanner model were identical to those in healthy volunteers. High resolution CT (HRCT) images were acquired

11 weeks after the MRI examination for clinical purposes. HRCT images were acquired on a 64-slice scanner (Lightspeed VCT, GE Healthcare, Waukesha, WI, USA) utilizing a 1.25 mm slice thickness, 120 kVp, 65.78 dose length product (~1.1 mSv dose), and reconstructed with an edge-preserving kernel at a 0.7 mm nominal in-plane spatial resolution.

RESULTS

Simulation and Phantom Studies

Figure 3 shows phantom images and simulations resulting from variable density and trapezoidal gradients. *T*2* was measured to be 0.53 ± 0.07, 0.99 ± 0.08, 1.65 ± 0.11, 3.1 ± 0.21, and 11.6 ± 0.69 ms for the five vials. *R*2* was homogenous across the fluid-filled vials and was strongly correlated with concentration ($r = 0.98$) with a *R*2* relaxivity of 7.5 mM^{-1} s^{-1}. In UTE images reconstructed using the first echo, short *T*2* vials were well visualized with both sampling techniques. For vials containing long *T*2* fluid, limited differences between the two sampling patterns were seen. However, short *T*2* vials exhibited higher SNR and less blurring with variable density sampling, matching the results of numerical simulation. The edge width was found to be relatively constant until *T*2* became shorter than the readout length. Measured edge widths of the phantoms were larger than predicted by the simulations. This was likely due to off-resonance blurring that was neither accounted for in simulations nor corrected for in reconstructions. Digital simulations and experiment were in agreement for SNR, which was found to be higher with variable density sampling for all *T*2* values. The largest improvement was found for the shorter *T*2* values, with a 67% gain for the shortest *T*2* phantom (0.53 ms). For the long *T*2* phantom, (not shown in plots) the variable density gradients still improved SNR by 31%.

Selective RF Pulses

The minimum phase RF pulses required a maximum B1 of 10.3 μT for a 6° flip angle and 300 μs pulse width. For the same max B1 and flip angle, 38 μs were required for the same excitation with a hard pulse. Figure 4a shows the effective flip angle as a function of pulse width for minimum phase SLR, sinc, and hard pulses. With a 300 μs pulse duration, excitation flip angles were 5.85° , 5.96° , and 5.48° for SLR, sinc, and hard pulses respectively. Figure 4b shows corresponding signal at the end of the RF pulse as function of pulse width. Signal levels with a 300 μs pulse duration were 92.5%, 73.5%, and 75.3% for SLR, sinc, and hard pulses respectively. Despite achieving the highest flip angle, sinc pulses consistently resulted in the lower signal. For a given pulse width, minimum phase RF pulses consistently resulted in higher signal and hard pulses resulted in lower signal. However, for the same max B1, hard pulses were more efficient. The 38μs hard pulse with the same max B1 as the 300 μs SLR had a higher signal at the end of the RF, 97.1% vs. 92.5%.

Figure 4c,d shows the flip angle and signal profile for the minimum phase SLR pulse. Outer volume excitation and profile broadening is observed as the RF pulse length increases. Despite outer volume excitation, limited signal is detectable from outside the selected volume as shown in Figure 4d. This is due to the incoherent phase of the excited spins. The signal fractional transition width increased with pulse length and was measured to be 0.09, 0.12, 0.27, and 0.62 for 10 μs, 300 μs, 1 ms, and 5 ms pulses respectively. For the same

pulse widths, sinc signal profiles were substantially wider with fractional transition widths of 0.25, 0.25, 0.27, and not measurable for 5 ms pulse due to limited signal.

Human Comparison Study

Average scan times across all 15 scans was 9:22 min (8:42–9:27 min), corresponding to an average respiratory efficiency of 50.3%. Discrepancies from the prescribed scan time arise from the 10 s lag required to adapt to abrupt changes in breathing patterns. Quantitative normalized contrast ratios (C_R) were 3.3% ± 2.8% for hard pulse RF with trapezoid readout, 7.8% ± 3.7% for selec tive RF pulse with trapezoid readout, and 12.7% ± 2.8% for selective RF pulse with variable density readout acquisitions. The contrast ratio for selective RF pulse with variable density readout was statistically higher than both hard pulse RF excitation with trapezoid readout ($P < 0.027$) and selective RF excitation with trapezoid readout ($P < 0.022$). However, no statistical difference was observed between the selective and non-selective trapezoid readout based acquisitions ($P = 0.25$). Apparent signal to noise ratios (S_R) were 4.6 ± 0.7, 6.6 ± 1.1, and 9.5 ± 2.1 for hard excitation with trapezoid, selective excitation with trapezoid, and selective excitation with variable density examinations. Selective excitation with variable density gradients resulted statistically higher apparent SNR than both selective ($P < 0.013$) and nonselective ($P < 0.008$) excitation with trapezoids. Additionally, selective excitation with trapezoids resulted in a higher apparent apparent SNR than non-selective excitation ($P < 0.003$).

Figure 5 summarizes results from the reader study with statistical differences noted. Significantly increased artifacts and/or noise were found when trapezoid gradients were utilized, as highlighted in Figure 6a, where signal from the abdomen aliases into the imaging volume resulting in substantial streak artifacts. This is dramatically improved with the addition of selective excitation and radial oversampling (Fig. 6b). The SNR is further improved with the incorporation of variable density readout gradients (Fig. 6c), allowing the visualization of interlobar fissures (arrows). Both selective and nonselective trapezoid readouts suffered from streaks/artifacts.

Airways were generally well visualized with all acquisitions; although subsegmental airways were better visualized with variable density sampling. This is highlighted in axial images shown in Figure 7. A small airway not visible with the hard pulse RF excitation trapezoid readout is visible in both acquisitions using the selective RF excitation, but the bronchial wall is better visualized with variable density sampling (Fig. 7b vs. Fig. 7c). Lung tissue image quality scores were statistically higher with variable density readouts, with excellent image quality in four of the five volunteers. Cardiac motion artifacts were almost completely mitigated with these highly averaged acquisitions, with no statistical difference between the three methods tested.

Feasibility in Interstitial Fibrosis

Figure 8 shows 3D reformations of HRCT, 3D UTE, and the second echo from the 3D UTE sequence. HRCT images do have higher apparent spatial resolution than the MRI images, allowing improved visualization of airways and fissures. However, both CT (Fig. 8a) and 3D UTE (Fig. 8b) show advanced interstitial fibrosis with honeycombing, consistent with

usual interstitial pneumonia (UIP). The same findings are much less visible on the later echo time images, which grossly underestimates the extent of fibrosis.

DISCUSSION

In this work, we demonstrate the feasibility of free-breathing 3D radial UTE whole lung imaging with a 1.25 mm isotropic resolution comparable with CT. The proposed technique utilized a variable density readout gradient which increased SNR levels of short *T*2* species by as much as 67% in phantom studies and provided significantly improved image quality in human volunteers. Techniques to limit the FOV were found to be essential to mitigate artifacts. The appearance of these artifacts was pronounced on superior lung segments and often present but not obvious on inferior sections. With an adaptive respiratory gating scheme, we were able to perform free-breathing scans without interrupting the steady state acquisition. This increased SNR through signal averaging without causing significant artifacts or incurring detectable blurring. With this optimized 3D UTE pulse sequence many lung features were well visualized, including fissures and airway walls.

UTE MR lung imaging has had a long history of development, but its clinical impact to date has been low. The proposed technique mitigates many of the image quality issues that have heretofore limited UTE imaging and may enable the development of clinically useful structural lung imaging with MRI. Compared to previous 2D techniques (11,12), 3D UTE approach is less sensitive to blood inflow, requires a single excitation, and provides whole chest coverage. In addition, the 3D UTE technique proposed here requires no hardware modifications and allows for simple large volume prescription on a commercially available MR scanner. This is in contrast to SWIFT and ZTE based techniques, which require hardware modifications to enable rapid RF switching critical to maintain SNR levels (58). Furthermore, selective excitation, which was shown to substantially improve image quality, is not currently feasible with ZTE and SWIFT based techniques. Compared to 3D UTE sequences shown in small animal studies, the proposed sequence provides higher SNR efficiency, selective excitation, and has now been shown to be feasible in normal human volunteers with physiologic conscious breathing patterns. Additionally, we utilized gradient calibrations to correct for *k*-space trajectory deviations, a well-known cause of errors in non-Cartesian acquisitions; this correction has been ignored in many previous 2D and 3D UTE techniques.

Substantial development is still needed to verify the efficacy and robustness of the proposed 3D UTE sequence in patients with lung disease. In this study, we have imaged a limited number of healthy human subjects and a single patient with interstitial fibrosis, which may not be representative of clinical patients. Patients, for example, are expected to have a substantially wider range of breathing patterns than observed. Additionally, respiratory gating currently relies on input from a respiratory bellows, which can exhibit poor coupling with lung volume in obese patients. Data-driven respiratory metrics using the center of *k*-space (59,60) may provide improved fidelity, but these techniques are designed for retrospective gating and will require more extensive changes for prospective sequences that sample *k*-space more uniformly. Despite respiratory gating, the acquisition remains sensitive to bulk motion during the scan. With the current axial selective RF excitation, the sequence

is particularly sensitive to motion of the patient's arms, which may create artifacts in the images. Future studies will determine the efficacy of respiratory gating in a larger clinical population and compare the bellows to data driven self-gating approaches.

The performance of UTE MRI in pathological conditions of the lung is still relatively unexplored. In our exams, we were able to visualize lobar lung fissures and demonstrated similar findings to CT in a single patient with interstitial fibrosis. However, it is unknown whether the UTE sampling will be sufficient to visualize structures typically seen with CT such as pulmonary edema, lung nodules, air trapping, or early stage interstitial fibrosis. The MR tissue properties, including *T*2*, of diseased human lungs are relatively unstudied. Studies in animals suggest that *T*2*, specifically, will be reduced in diseases such as emphysema (31,61). Many lung diseases replace air with soft tissue or fluid, which should prove to be beneficial for *T*2* weighted MR imaging with this new UTE method. However, with reduced *T*2* values, the 1ms readout utilized may be suboptimal. With shorter readout windows, the SNR gains from variable density sampling will be reduced. The different relaxation times of blood, pulmonary edema, malignancy and purulent material may also offer a multiparametric imaging data set for clinical analysis to further help characterize lung diseases that now are simply seen as a high attenuation areas on CT. All of our scans were performed on a 3T system where the *T*2* is substantial shorter than at 1.5 T. Subsequently, the use of lower field scanners may allow for improved characterization of lung tissue with pathologically shortened *T*2*.

CONCLUSION

In this work, we demonstrated the feasibility of free-breathing 3D radial UTE whole lung imaging. We demonstrate improved image quality after incorporating a variable density readout gradient, respiratory gating, and techniques to limit the FOV. These improvements improve the apparent SNR, reduce obscuring artifacts, and allowed visualization of lung parenchyma, airways, and fissures.

Acknowledgments

The authors acknowledge research support from GE Healthcare and The Hartwell Foundation. The content is solely the responsibility of the authors and does not necessarily represent the official views of the NIH.

Grant sponsor: NIH; Grant numbers: R01NS066982, R01HL072260-05; Grant sponsor: National Center for Research Resources; Grant number: 1UL1RR025011; Grant sponsor: National Center for Advancing Translational Sciences; Grant number: 9U54TR000021; Grant sponsor: UW School of Medicine and Public Health.

REFERENCES

1. Kauczor H, Surkau R, Roberts T. MRI using hyperpolarized noble gases. Eur Radiol. 1998; 8:820–827. [PubMed: 9601972]
2. Chen XJ, Hedlund LW, Moller HE, Chawla MS, Maronpot RR, Johnson GA. Detection of emphysema in rat lungs by using magnetic resonance measurements of 3He diffusion. Proc Natl Acad Sci U S A. 2000; 97:11478–11481. [PubMed: 11027348]
3. Kaushik SS, Cleveland ZI, Cofer GP, et al. Diffusion-weighted hyper-polarized 129Xe MRI in healthy volunteers and subjects with chronic obstructive pulmonary disease. Magn Reson Med. 2011; 65:1154–1165. [PubMed: 21413080]

4. Mugler JP III, Driehuys B, Brookeman JR, et al. MR imaging and spectroscopy using hyperpolarized 129Xe gas: preliminary human results. Magn Reson Med. 1997; 37:809–815. [PubMed: 9178229]
5. Ohno Y, Hatabu H, Murase K, Higashino T, Nogami M, Yoshikawa T, Sugimura K. Primary pulmonary hypertension: 3D dynamic perfusion MRI for quantitative analysis of regional pulmonary perfusion. AJR Am J Roentgenol. 2007; 188:48–56. [PubMed: 17179345]
6. Mai VM, Berr SS. MR perfusion imaging of pulmonary parenchyma using pulsed arterial spin labeling techniques: FAIRER and FAIR. J Magn Reson Imaging. 1999; 9:483–487. [PubMed: 10194721]
7. Sanz J, Kuschnir P, Rius T, Salguero R, Sulica R, Einstein AJ, Dellegrottaglie S, Fuster V, Rajagopalan S, Poon M. Pulmonary arterial hypertension: Noninvasive detection with phase-contrast MR imaging. Radiology. 2007; 243(1):70–79. [PubMed: 17329691]
8. Pullinger B, Profka H, Ardenkjaer-Larsen JH, Kuzma NN, Kadlecek S, Rizi RR. Metabolism of hyperpolarized [1–13C]pyruvate in the isolated perfused rat lung—An ischemia study. NMR Biomed. 2012; 25:1113–1118. [PubMed: 22311307]
9. Ebner B, Behm P, Jacoby C, Burghoff S, French BA, Schrader J, Flogel U. Early assessment of pulmonary inflammation by 19F MRI in vivo. Circ Cardiovasc Imaging. 2010; 3:202–210. [PubMed: 20061515]
10. Strobel K, Hoerr V, Schmid F, Wachsmuth L, Löffler B, Faber C. Early detection of lung inflammation: Exploiting T1-effects of iron oxide particles using UTE MRI. Magn Reson Med. 2012; 68:1924–1931. [PubMed: 22368111]
11. Stock KW, Chen Q, Hatabu H, Edelman RR. Magnetic resonance T2* measurements of the normal human lung in vivo with ultra-short echo times. Magn Reson Imaging. 1999; 17:997–1000. [PubMed: 10463650]
12. Yu J, Xue Y, Song HK. Comparison of lung T2* during free-breathing at 1.5 T and 3.0 T with ultrashort echo time imaging. Magn Reson Med. 2011; 66:248–254. [PubMed: 21695727]
13. Theilmann RJ, Arai TJ, Samiee A, Dubowitz DJ, Hopkins SR, Buxton RB, Prisk GK. Quantitative MRI measurement of lung density must account for the change in T(2) (*) with lung inflation. J Magn Reson Imaging. 2009; 30:527–534. [PubMed: 19630079]
14. Hatabu H, Alsop DC, Listerud J, Bonnet M, Gefter WB. T2* and proton density measurement of normal human lung parenchyma using submillisecond echo time gradient echo magnetic resonance imaging. Eur J Radiol. 1999; 29:245–252. [PubMed: 10399610]
15. Ohno Y, Koyama H, Yoshikawa T, Matsumoto K, Takahashi M, Van Cauteren M, Sugimura K. T2* measurements of 3-T MRI with ultra-short TEs: Capabilities of pulmonary function assessment and clinical stage classification in smokers. AJR Am J Roentgenol. 2011; 197:W279–W285. [PubMed: 21785054]
16. Mayo JR, MacKay A, Muller NL. MR imaging of the lungs: value of short TE spin-echo pulse sequences. AJR Am J Roentgenol. 1992; 159:951–956. [PubMed: 1414805]
17. Bergin CJ, Pauly JM, Macovski A. Lung parenchyma: Projection reconstruction MR imaging. Radiology. 1991; 179:777–781. [PubMed: 2027991]
18. Ohno Y, Koyama H, Yoshikawa T, et al. N stage disease in patients with non-small cell lung cancer: efficacy of quantitative and qualitative assessment with STIR turbo spin-echo imaging, diffusion-weighted MR imaging, and fluorodeoxyglucose PET/CT. Radiology. 2011; 261:605–615. [PubMed: 21926377]
19. Lutterbey G, Gieseke J, von Falkenhausen M, Morakkabati N, Schild H. Lung MRI at 3.0 T: A comparison of helical CT and high-field MRI in the detection of diffuse lung disease. Eur Radiol. 2005; 15:324–328. [PubMed: 15565313]
20. Hatabu H, Gaa J, Tadamura E, Edinburgh KJ, Stock KW, Garpestad E, Edelman RR. MR imaging of pulmonary parenchyma with a half-Fourier single-shot turbo spin-echo (HASTE) sequence. Eur J Radiol. 1999; 29:152–159. [PubMed: 10374663]
21. Idiyatullin D, Corum C, Park JY, Garwood M. Fast and quiet MRI using a swept radiofrequency. J Magn Reson. 2006; 181:342–349. [PubMed: 16782371]
22. Weiger M, Hennel F, Pruessmann KP. Sweep MRI with algebraic reconstruction. Magn Reson Med. 2010; 64:1685–1695. [PubMed: 20949600]

23. Wu Y, Dai G, Ackerman JL, Hrovat MI, Glimcher MJ, Snyder BD, Nazarian A, Chesler DA. Water- and fat-suppressed proton projection MRI (WASPI) of rat femur bone. Magn Reson Med. 2007; 57:554–567. [PubMed: 17326184]
24. Balcom BJ, Macgregor RP, Beyea SD, Green DP, Armstrong RL, Bremner TW. Single-point ramped imaging with T1 enhancement (SPRITE). J Magn Reson A. 1996; 123:131–134. [PubMed: 8980075]
25. Grodzki DM, Jakob PM, Heismann B. Ultrashort echo time imaging using pointwise encoding time reduction with radial acquisition (PETRA). Magn Reson Med. 2012; 67:510–518. [PubMed: 21721039]
26. Qian Y, Boada FE. Acquisition-weighted stack of spirals for fast high-resolution three-dimensional ultra-short echo time MR imaging. Magn Reson Med. 2008; 60:135–145. [PubMed: 18581326]
27. Kuethe DO, Adolphi NL, Fukushima E. Short data-acquisition times improve projection images of lung tissue. Magn Reson Med. 2007; 57:1058–1064. [PubMed: 17534926]
28. Togao O, Tsuji R, Ohno Y, Dimitrov I, Takahashi M. Ultrashort echo time (UTE) MRI of the lung: Assessment of tissue density in the lung parenchyma. Magn Reson Med. 2010; 64:1491–1498. [PubMed: 20574988]
29. Zurek M, Bessaad A, Cieslar K, Cremillieux Y. Validation of simple and robust protocols for high-resolution lung proton MRI in mice. Magn Reson Med. 2010; 64:401–407. [PubMed: 20665784]
30. Togao O, Ohno Y, Dimitrov I, Hsia CC, Takahashi M. Ventilation/perfusion imaging of the lung using ultra-short echo time (UTE) MRI in an animal model of pulmonary embolism. J Magn Reson Imaging. 2011; 34:539–546. [PubMed: 21761465]
31. Takahashi M, Togao O, Obara M, van Cauteren M, Ohno Y, Doi S, Kuro-o M, Malloy C, Hsia CC, Dimitrov I. Ultra-short echo time (UTE) MR imaging of the lung: comparison between normal and emphysematous lungs in mutant mice. J Magn Reson Imaging. 2010; 32:326–333. [PubMed: 20677258]
32. Jakob PM, Hillenbrand CM, Wang T, Schultz G, Hahn D, Haase A. Rapid quantitative lung (1)H T(1) mapping. J Magn Reson Imaging. 2001; 14:795–799. [PubMed: 11747038]
33. Schmidt MA, Yang GZ, Keegan J, Jhooti P, Gatehouse PD, Carr DH, Hansell DM, Firmin DN. Non-breath-hold lung magnetic resonance imaging with real-time navigation. Magma. 1997; 5:123–128. [PubMed: 9268076]
34. Barger AV, Block WF, Toropov Y, Grist TM, Mistretta CA. Time-resolved contrast-enhanced imaging with isotropic resolution and broad coverage using an undersampled 3D projection trajectory. Magn Reson Med. 2002; 48:297–305. [PubMed: 12210938]
35. Liao JR, Pauly JM, Brosnan TJ, Pelc NJ. Reduction of motion artifacts in cine MRI using variable-density spiral trajectories. Magn Reson Med. 1997; 37:569–575. [PubMed: 9094079]
36. Johnson, KM.; Lum, D.; Francois, C.; Reeder, S.; Busse, RF.; Grist, TM.; Wieben, O. Non-contrast enhanced MR angiography with PC VIPR.. Proceedings of the 16th Annual Meeting of ISMRM; Toronto, Canada. 2008; p. 733
37. Francois CJ, Lum DP, Johnson KM, Landgraf BR, Bley TA, Reeder SB, Schiebler ML, Grist TM, Wieben O. Renal arteries: Isotropic, high-spatial-resolution, unenhanced MR angiography with three-dimensional radial phase contrast. Radiology. 2011; 258:254–260. [PubMed: 20980449]
38. McConnell MV, Khasgiwala VC, Savord BJ, Chen MH, Chuang ML, Edelman RR, Manning WJ. Comparison of respiratory suppression methods and navigator locations for MR coronary angiography. AJR Am J Roentgenol. 1997; 168:1369–1375. [PubMed: 9129447]
39. Pauly, JM.; Connelly, SM.; Nishimura, DG.; Macovski, A. Slice selectivity for very short T2 Species.; Proceedings of SMRM; Amsterdam, The Netherlands. 1989; p. 28
40. Wansapura JP, Daniel BL, Pauly J, Butts K. Temperature mapping of frozen tissue using eddy current compensated half excitation RF pulses. Magn Reson Med. 2001; 46:985–992. [PubMed: 11675651]
41. Josan S, Kaye E, Pauly JM, Daniel BL, Pauly KB. Improved half RF slice selectivity in the presence of eddy currents with out-of-slice saturation. Magn Reson Med. 2009; 61:1090–1095. [PubMed: 19319972]

42. Nagel AM, Laun FB, Weber MA, Matthies C, Semmler W, Schad LR. Sodium MRI using a density-adapted 3D radial acquisition technique. Magn Reson Med. 2009; 62:1565–1573. [PubMed: 19859915]
43. Star-Lack JM. Optimal gradient waveform design for projection imaging and projection reconstruction echoplanar spectroscopic imaging. Magn Reson Med. 1999; 41:664–675. [PubMed: 10332841]
44. Mir R, Guesalaga A, Spiniak J, Guarini M, Irarrazaval P. Fast three-dimensional k-space trajectory design using missile guidance ideas. Magn Reson Med. 2004; 52:329–336. [PubMed: 15282815]
45. Konstandin S, Nagel AM, Heiler PM, Schad LR. Two-dimensional radial acquisition technique with density adaption in sodium MRI. Magn Reson Med. 2011; 65:1090–1096. [PubMed: 21413073]
46. Konstandin S, Nagel AM. Performance of sampling density-weighted and postfiltered density-adapted projection reconstruction in sodium magnetic resonance imaging. Magn Reson Med. 2013; 69:495–502. [PubMed: 22473708]
47. Lustig M, Kim SJ, Pauly JM. A fast method for designing time-optimal gradient waveforms for arbitrary k-space trajectories. IEEE Trans Med Imaging. 2008; 27:866–873. [PubMed: 18541493]
48. Lu A, Atkinson IC, Claiborne TC, Damen FC, Thulborn KR. Quantitative sodium imaging with a flexible twisted projection pulse sequence. Magn Reson Med. 2010; 63:1583–1593. [PubMed: 20512862]
49. Duyn JH, Yang YH, Frank JA, van der Veen JW. Simple correction method for k-space trajectory deviations in MRI. J Magn Reson. 1998; 132:150–153. [PubMed: 9615415]
50. Gurney, P.; Pauly, J.; Nishimura, DG. A simple method for measuring B0 eddy currents.. Proceedings of the 14th Annual Meeting of ISMRM; Seattle, Washington, USA. 2005; p. 866
51. Larson PE, Gurney PT, Nayak K, Gold GE, Pauly JM, Nishimura DG. Designing long-T2 suppression pulses for ultrashort echo time imaging. Magn Reson Med. 2006; 56:94–103. [PubMed: 16724304]
52. Robson MD, Gatehouse PD. Consequences of T2 relaxation during half-pulse slice selection for ultrashort TE imaging. Magn Reson Med. 2010; 64:610–615. [PubMed: 20665804]
53. Springer F, Steidle G, Martirosian P, Claussen CD, Schick F. Effects of in-pulse transverse relaxation in 3D ultrashort echo time sequences: Analytical derivation, comparison to numerical simulation and experimental application at 3T. J Magn Reson. 2010; 206:88–96. [PubMed: 20637661]
54. Carl M, Bydder M, Du J, Takahashi A, Han E. Optimization of RF excitation to maximize signal and T2 contrast of tissues with rapid transverse relaxation. Magn Reson Med. 2010; 64:481–490. [PubMed: 20665792]
55. Beatty PJ, Nishimura DG, Pauly JM. Rapid gridding reconstruction with a minimal oversampling ratio. IEEE Trans Med Imaging. 2005; 24:799–808. [PubMed: 15959939]
56. Pruessmann KP, Weiger M, Bornert P, Boesiger P. Advances in sensitivity encoding with arbitrary k-space trajectories. Magn Reson Med. 2001; 46:638–651. [PubMed: 11590639]
57. McKenzie CA, Yeh EN, Ohliger MA, Price MD, Sodickson DK. Self-calibrating parallel imaging with automatic coil sensitivity extraction. Magn Reson Med. 2002; 47:529–538. [PubMed: 11870840]
58. Weiger M, Pruessmann KP, Hennel F. MRI with zero echo time: hard versus sweep pulse excitation. Magn Reson Med. 2011; 66:379–389. [PubMed: 21381099]
59. Brau AC, Brittain JH. Generalized self-navigated motion detection technique: Preliminary investigation in abdominal imaging. Magn Reson Med. 2006; 55:263–270. [PubMed: 16408272]
60. Larson AC, White RD, Laub G, McVeigh ER, Li D, Simonetti OP. Self-gated cardiac cine MRI. Magn Reson Med. 2004; 51:93–102. [PubMed: 14705049]
61. Olsson LE, Lindahl M, Onnervik PO, Johansson LB, Palmer M, Reimer MK, Hultin L, Hockings PD. Measurement of MR signal and T2* in lung to characterize a tight skin mouse model of emphysema using single-point imaging. J Magn Reson Imaging. 2007; 25:488–494. [PubMed: 17279537]

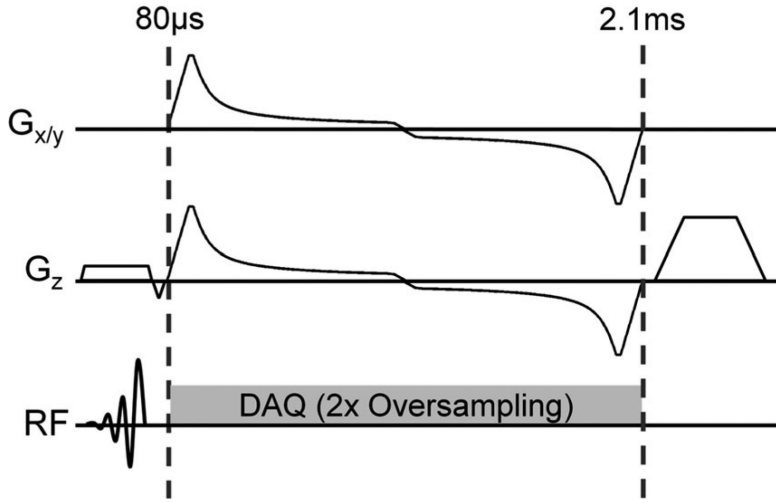

FIG. 1.

Pulse sequence diagram for dual-echo variable density 3D UTE consisting of short (high bandwidth) slab excitation, an arc-length optimized out-and-back radial readout utilizing variable gradients, followed by a gradient spoiler.

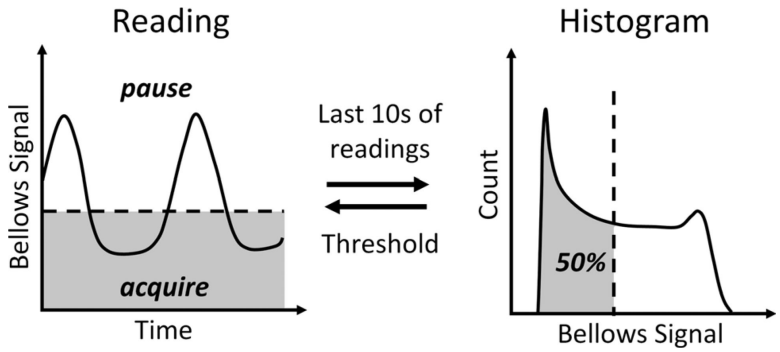

FIG. 2.

Respiratory motion can be minimized with real-time gating to end-expiration through adaptive feedback from the respiratory bellows signal with a 50% acceptance window (shaded in gray).

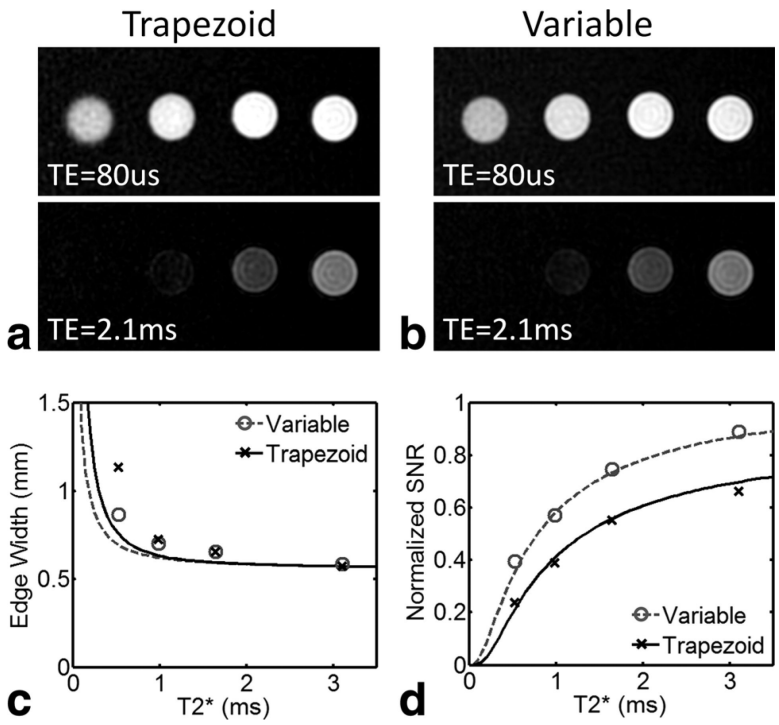

FIG. 3.

Phantom images acquired with trapezoidal gradients (**a**) and variable density gradients (**b**) with vials arranged left to right from short to long *T*2* (0.53–3.1 ms). Note the longest *T*2* phantom (11.6 ms) is not shown for brevity. Note the increase in noise and decrease in edge sharpness in the short *T*2* vials. Similar trends are observed in experimental and theoretical measures for edge width (**c**), and SNR (**d**). For the shortest *T*2* species (*T*2* = 0.53 ms) there is a 67% gain in SNR with variable density sampling compared with ramp sampled trapezoidal gradients. Disagreement in edge width likely arises from off-resonance effects that were not included in the theoretical model.

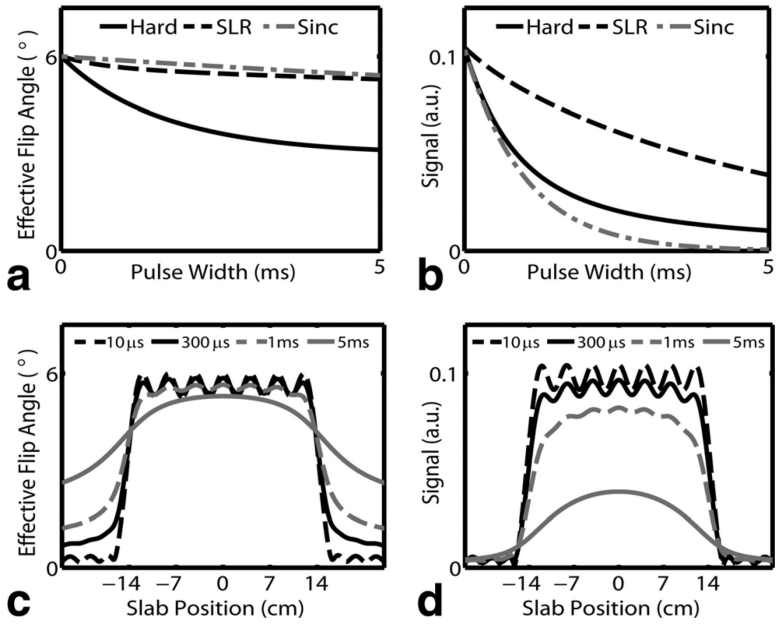

FIG. 4.

Effective flip angle (**a**) and signal at end of RF (**b**) for hard, SLR, and symmetric Sinc pulses as a function of pulse width. *T*2 was fixed at 0.5 ms. The effective flip angle is dominated by RF bandwidth effects and is largely independent of the pulse shape. However, signal is highly sensitive to RF shape due to signal decay during the RF pulse and is substantially higher for SLR pulses. The flip angle excitation profiles for SLR pulses (**c**) shows accurate inner volume excitation with outer volume excitation apparent with long RF pulses. Outer volume signal rapidly decays and is not detectable in the signal (**d**). Signal broadening occurs with long RF pulses.

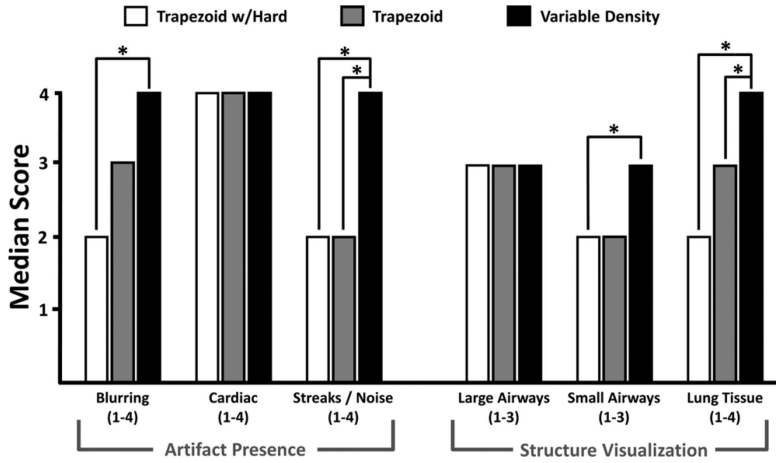

FIG. 5.

Scoring results from the consensus reader study of the five normal volunteers with statistical differences noted ($P < 0.05$). Consistent improvement in image quality was found with variable density readout gradients.

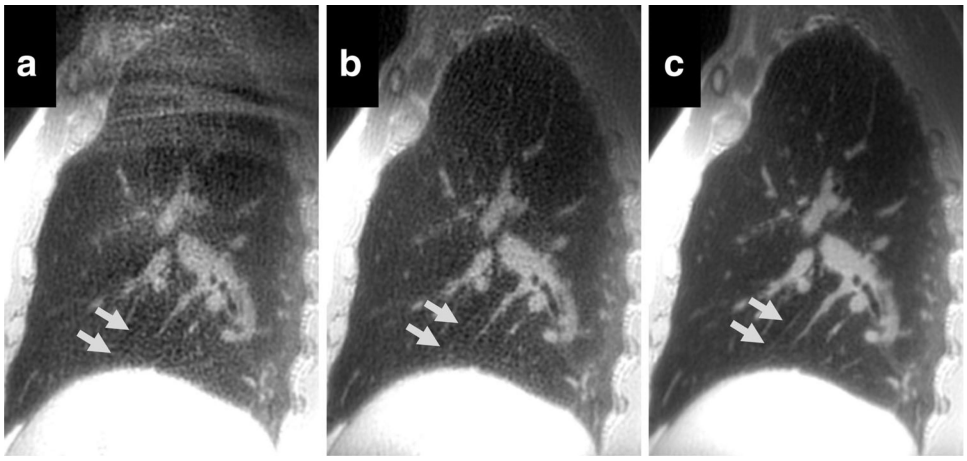

FIG. 6.

Sagittal reformats of a 3D UTE from the same volunteer acquired with a hard RF pulse with trapezoid readout (**a**), selective RF pulse with trapezoid readout (**b**), and selective RF pulse with variable density readout (**c**). Severe artifacts are visible superiorly due to wrap from outside the FOV in (a) overlying the right upper lobe. Arrows show the right major fissure with progressive improvement in its visibility with this optimized UTE technique.

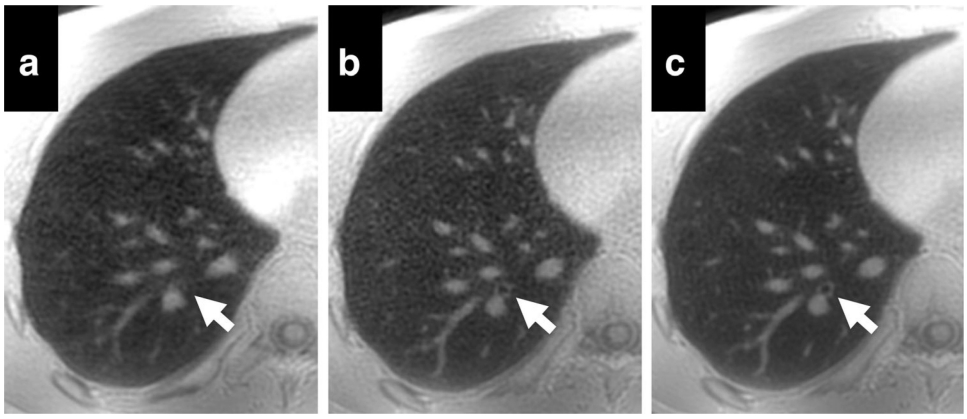

FIG. 7.

Axial reformats of a 3D UTE from a volunteer acquired with a hard RF pulse with trapezoid readout (**a**), selective RF pulse with trapezoid readout (**b**), and selective RF pulse with variable density readout (**c**). Arrows point to a small subsegmental airway. This airway is obscured by artifacts in the acquisition using a hard pulse RF excitation. The bronchial wall is visible on both acquisitions with selective excitation, with slightly higher quality in the variable density acquisition. Note the generalized improvement in overall image quality from left to right.

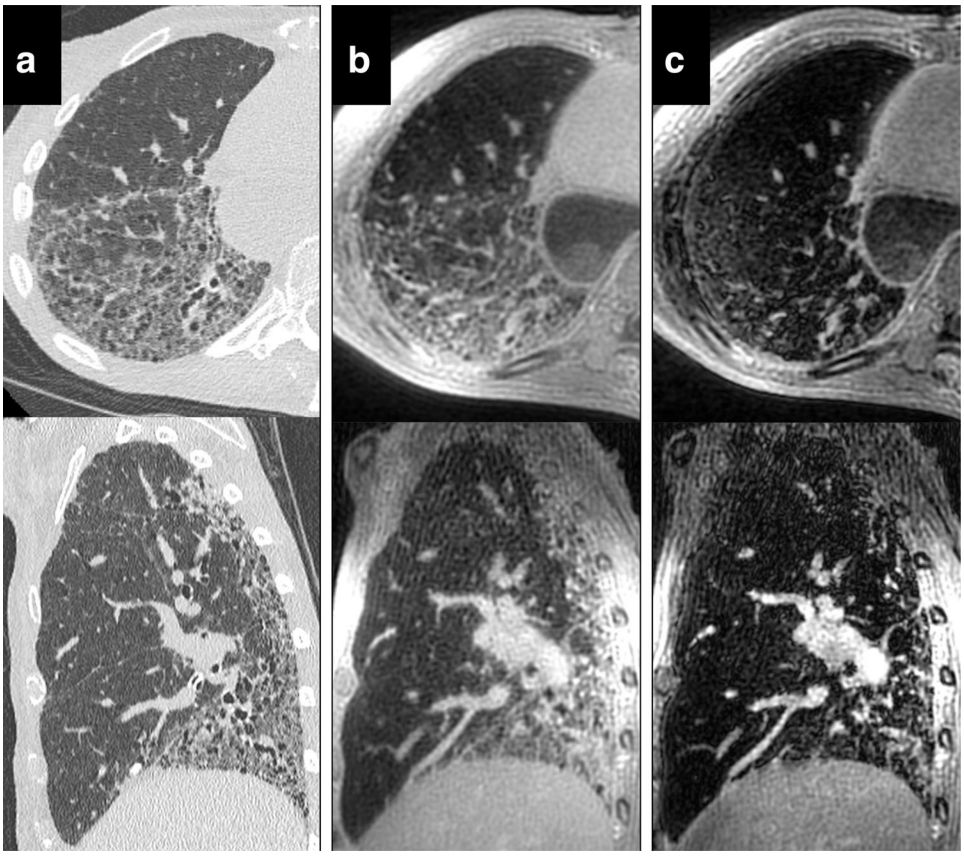

FIG. 8.

Axial and sagittal reformats of HRCT (**a**), 3D UTE (**b**), and the second echo of the 3D UTE sequence (TE = 2.1 ms). HRCT was performed 11 weeks after the 3D UTE scan. Both HRCT and 3D UTE scans show similar fibrosis patterns and extent, which is not well visualized in late echo MRI images. HRCT images show substantially higher spatial resolution, likely due to higher nominal resolution and reduced respiratory motion.

Table 1

Likert Scales for Qualitative Scoring for the Three Acquisitions in Each Healthy Subject

Categories	Description	Score
Artifacts (blurring, cardiac motion, streaks and noise)	Severe – Renders images non-diagnostic	1
	Moderate – Obscures lung anatomy	2
	Mild – Present but does not obscure lung anatomy	3
	Minimal/none	4
Lung tissue signal	None – Indistinguishable from air	1
	Minimal – Barely distinguishable from air	2
	Good – Clearly distinguishable from air, but fissures not visible	3
	Excellent – Clearly distinguishable from air, with lung fissures visible.	4
Airways (large, small)	Poor – Indistinguishable from nearby lung tissue	1
	Fair – Lower signal than nearby lung tissue	2
	Good – Lower signal than nearby lung tissue and bronchial wall visible	3